Bioactive Materials 12 (2022) 246–256

Contents lists available at ScienceDirect

Bioactive Materials

journal homepage: www.keaipublishing.com/en/journals/bioactive-materials

Ultrasmall Fe-doped carbon dots nanozymes for photoenhanced antibacterial therapy and wound healing

Yunhang Liu [a,1], Bolong Xu [a,1], Mingzhu Lu [a], Shanshan Li [a], Juan Guo [a], Fangzhou Chen [b], Xiaolu Xiong [b], Zhe Yin [b], Huiyu Liu [a,*], Dongsheng Zhou [b,**]

[a] Beijing Advanced Innovation Center for Soft Matter Science and Engineering, State Key Laboratory of Organic-Inorganic Composites, Bionanomaterials & Translational Engineering Laboratory, Beijing Key Laboratory of Bioprocess, Beijing Laboratory of Biomedical Materials, Beijing University of Chemical Technology, Beijing, 100029, China

[b] State Key Laboratory of Pathogen and Biosecurity, Beijing Institute of Microbiology and Epidemiology, Beijing, 100071, China

ARTICLE INFO

Keywords:
Carbon dots
Nanozymes
Photothermal effect
Antibacterial therapy
Wound healing

ABSTRACT

Pathogenic bacteria pose a devastating threat to public health. However, because of the growing bacterial antibiotic resistance, there is an urgent need to develop alternative antibacterial strategies to the established antibiotics. Herein, iron-doped carbon dots (Fe-CDs, ~3 nm) nanozymes with excellent photothermal conversion and photoenhanced enzyme-like properties are developed through a facile one-pot pyrolysis approach for synergistic efficient antibacterial therapy and wound healing. In particular, Fe doping endows CDs with photoenhanced peroxidase (POD)-like activity, which lead to the generation of heat and reactive oxygen species (ROS) for Gram-positive and Gram-negative bacteria killing. This study demonstrates Fe-CDs have significant wound healing efficiency of Fe-CDs by preventing infection, promoting fibroblast proliferation, angiogenesis, and collagen deposition. Furthermore, the ultrasmall size of Fe-CDs possesses good biocompatibility favoring clinical translation. We believe that the nanozyme-mediated therapeutic platform presented here is expected to show promising applications in antibacterial.

1. Introduction

Bacterial infection is the major restriction for wound management [1]. The increasing bacterial antibiotic resistance challenges the use of established antibiotics [2]. The exploration of alternative strategies to fight against bacterial infection is highly required.

Nanozymes, referring to nanoparticles with enzyme-like characteristics, are greatly promising in wound disinfection as non-antibiotic therapeutics [3,4]. For example, peroxidase (POD)-like mimics can convert hydrogen peroxide (H_2O_2) into highly active hydroxyl radicals (•OH), exerting toxic actions on bacteria and thus avoiding the occurrence of bacterial resistance. To date, many nanozymes have been employed for antibacterial therapy, including metal nanozymes [5,6], metal oxides or metal sulfides nanozymes [7,8], and carbon-based nanozymes [9,10]. Among these nanozymes, carbon-based nanozymes doped with N element are very attractive candidates, since N element in carbon-based nanozymes plays a vital role in the stabilization and bind of substrates, similar to the function of N in natural enzymes and cofactors [11]. Nevertheless, most of carbon matrix such as carbon nanotubes and graphene oxide suffers from the drawback of cytotoxic to normal cells and result in the apoptosis of cells [12,13].

Encouragingly, carbon dots (CDs) are a kind of 0-dimension nanomaterials with ultrasmall size below 10 nm, which have great potential for antibacterial therapy due to the outstanding optical properties, catalytic properties, and especially good biocompatibility features [14]. The ultrasmall size will endow CDs more exposed active sites and functional groups for modification. Besides, CDs can also be produced in a simple, environmentally friendly, and high-yield way [15–17]. However, the limited catalytic efficiency caused by the poor electron transfer efficiency inside the structure of CDs prevents their further application. Heteroatom doping is widely used to improve the internal electronic environment [18]. Recent researches showed that Fe doping would lead

Peer review under responsibility of KeAi Communications Co., Ltd.
* Corresponding author. Beijing University of Chemical Technology, Beijing 100029, China.
** Corresponding author. Beijing Institute of Microbiology and Epidemiology, Beijing 100071, China.
E-mail addresses: liuhy@mail.buct.edu.cn (H. Liu), dongshengzhou1977@gmail.com (D. Zhou).
[1] Yunhang Liu, Bolong Xu contributed equally to this work.

https://doi.org/10.1016/j.bioactmat.2021.10.023
Received 8 July 2021; Received in revised form 18 October 2021; Accepted 18 October 2021
Available online 25 October 2021

to higher utilization of active sites throughout the POD-like catalytic process, and Fe doped carbon nanozyme exhibits higher enzyme-like activity than other metal doped carbon (ie., Mn, Co, Ni, Cu) nanozymes [19,20]. Thus, doping Fe into CDs is an appealing approach to increase the enzyme-like activity. Such heteroatom doping could not only change the internal electronic environment but also provide active sites and endow CDs with novel functions. In addition, CDs with strong absorbance in the near-infrared (NIR) region are potential to act as photothermal agent for photothermal therapy (PTT), which is also promise to promote the electron transfer efficiency by thermal field, thus enhance the enzyme-like activity [21]. Therefore, the photothermal effect and photoenhanced enzyme-like activity of CDs are expected to achieve highly efficient antibacterial efficiency.

Herein, we prepared iron-doped carbon dots (Fe-CDs) with an average size of about 3 nm by a facile one-pot pyrolysis approach. Compared to pristine CDs, Fe-CDs possess prominent photoenhanced POD-like activity, which enables Fe-CDs a promising candidate for efficient wound healing. The Fe-CDs also show an excellent photothermal conversion performance (η = 35.11%), and excellent photostability under NIR laser irradiation. The photothermal effect produced by Fe-CDs upon NIR laser irradiation, not only induces the death of bacteria without causing damage to normal tissues but also enhances the catalytic efficiency of Fe-CDs. The in vitro antibacterial experiments display that Fe-CDs-based therapeutic platform possesses a great bactericidal effect on *Staphylococcus aureus* (*S. aureus*) and *Escherichia coli* (*E. coli*). Based on the proposed Fe-CDs-based therapeutic platform, we demonstrate that the healing process of the bacteria-infected wound model was significantly accelerated, as evidenced by promoting fibroblast proliferation, neovascularization, and collagen deposition. Importantly, the ultrasmall size Fe-CDs show good biocompatibility. The dual-purpose strategy provided by Fe-CDs opens an avenue to use biocompatible antibiotics-free nanomaterial for wound disinfection and healing.

2. Materials and methods

2.1. Materials

Ethylenediaminetetraacetic acid monosodium ferric salt (NaFeEDTA), ethylenediaminetetraacetic acid disodium salt dihydrate ($Na_2[H_2(EDTA)]\cdot 2H_2O$), and 3,3′,5,5′-tetramethylbenzidine (TMB) single-component substrate solution were obtained from Aladdin Chemistry Co., Ltd. Dialysis bag (MWCO = 3500 Da) was obtained from MYM Biological Technology Co., Ltd. H_2O_2 (30%) and TMB were obtained from Sigma-Aldrich. Methylene blue (MB) was obtained from Macklin. 2′,7′-dichlorofluorescein diacetate (DCFH-DA), SYTO-9, and PI were obtained from Roche Applied Science. 3-(4,5-Dimethylthiazol-2-yl)-2,5-diphenyltetrazolium bromide (MTT) assay and Dimethylsulfoxide (DMSO) were obtained from Solarbio Science & Technology Co., Ltd. All chemicals were used as received without further purification.

2.2. Characterization

Hitachi HT-7700 microscope at a working voltage of 100 kV and JEM-2100F microscope at a working voltage of 200 kV were used to characterize the morphology of CDs and Fe-CDs. Raman spectra were performed on LabRAM HR Evolution at a 514 nm excitation. Thermo Scientific NICOLET 6700 Fourier transform infrared (FT-IR) spectrometer was used to confirm the functional groups of CDs and Fe-CDs. Shimadzu X-ray diffraction (XRD)-6000 X-ray diffractometer was used to characterize the crystalline structures of CDs and Fe-CDs. ESCALab220i-XL high-performance electron spectrometer with a monochromatic Al Kα source was used to characterize the surface structure of CDs and Fe-CDs. Shimadzu UV-2600 spectrophotometer was used to record the UV–Vis–NIR spectra of CDs and Fe-CDs. Malvern Zetasizer Nano ZS was used to measure the zeta potential of as-prepared samples. S-4800 scanning electron microscope (SEM) was used to characterize the morphology of bacteria. The samples were prepared by dropping the bacterial suspension on the silicon wafer. Inductively coupled plasma mass spectrometry (ICP-MS) was used to detect the content of iron.

2.3. Preparation and purification of Fe-CDs and pristine CDs

Fe-CDs were prepared according to the previously reported method with some modifications [22]. In general, 2 g NaFeEDTA was filled smoothly in a quartz boat, and then pyrolyzed in a tube furnace at 350 °C under N_2 atmosphere for 2 h at a heating rate of 5 °C min^{-1}. After pyrolysis, 150 mL ultrapure water was added to dissolve the product. The suspension was treated with ultrasound for 15 min at room temperature. After that, a clear brown solution could be obtained after a high-speed centrifuging (11,000 rpm) for 20 min to remove the insoluble iron and sodium salts. Thereafter, a 0.22 μm membrane filter was used to filter the upper brown solution to remove carbon fragments. After that, the resulting solution was dialyzed against ultrapure water for 2 days to remove the small fragments and residual salts. Finally, pure brown Fe-CDs powder was acquired through lyophilization and stored for further use. Pure CDs were prepared using a similar method except that the precursor was $Na_2[H_2(EDTA)]\ 2H_2O$.

2.4. In vitro photothermal measurement

A series of Fe-CDs aqueous dispersions (1.0 mL) with different concentrations (12.5, 25, 50, 100, 200 and 400 μg mL^{-1}) as well as ultrapure water were prepared and irradiated with NIR laser (808 nm, 2 W cm^{-2}) for 10 min. The temperatures of the Fe-CDs were recorded through a thermocouple thermometer.

2.5. Peroxidase-like activity and kinetic assay of Fe-CDs

Shimadzu UV-2600 spectrophotometer was used to evaluate the POD-like activity of Fe-CDs. Specifically, Fe-CDs (final working concentrations: 100 μg mL^{-1}) was injected into HAc/NaAc buffer (0.1 M, pH = 6.5) involved of TMB single-component substrate solution (final system: 3 mL). The photo-enhanced POD-like activity was carried out by exposing to NIR laser irradiation (808 nm, 2 W cm^{-2}) for 5 min during the 10 min's reaction procedure with 1.0 mL system containing the same concentration of Fe-CDs and TMB single-component substrate solution. Kinetic assay was performed in 100 μL HAc/NaAc buffer, containing 200 μg mL^{-1} Fe-CDs, 1664 μM TMB, and different concentrations of H_2O_2 (0, 18.75, 37.5, 75, 150, 300, and 600 mM), or containing 200 μg mL^{-1} Fe-CDs, 150 mM H_2O_2, and different concentrations of TMB (0, 89.22, 166.4, 332.8, 666, 998, 1332, 1664 μM). All experiments were repeated three times. The Michaelis-Menten constant (K_m) and the maximum initial velocity (V_{max}) was calculated according to:

$$\frac{1}{V}=\frac{K_m}{V_{max}[S]}+\frac{1}{V_{max}}$$

Where V represents the initial reaction velocity, K_m represents the Michaelis constant, $[S]$ is the concentration of substrate, and V_{max} is the maximal reaction velocity.

2.6. Quantitative analysis of the generation of •OH

Terephthalic acid (TA) was used to detect •OH, which would show a highly fluorescent product 2-hydroxyterephtthalic acid. The experiments were accomplished in HAc/NaAc buffer (0.1 M, pH = 6.5) including TA, Fe-CDs, H_2O_2, TA + Fe-CDs, TA + H_2O_2 TA + Fe-CDs + H_2O_2, TA + Fe-CDs + H_2O_2 + NIR, respectively. The final concentration of TA, Fe-CDs, and H_2O_2 were 0.5 mM, 200 μg mL^{-1}, and 10 mM, respectively. After incubation 12 h, the fluorescence spectra of all groups were conducted.

The degradation of Methylene blue (MB) was also used to determine the generation of •OH through Shimadzu UV-2600 spectrophotometer. Specifically, Methylene blue (MB) (final working concentrations: 5 μg mL^{-1}) and Fe-CDs were added into HAc/NaAc buffer (0.1 M, pH = 6.5). With the addition of H_2O_2 (final working concentrations: 1 mM), the MB was degraded, and the MB was degraded more at the same time under NIR laser irradiation (808 nm, 2 W cm^{-2}). The absorbance changes of MB at 665 nm were measured.

2.7. Bacterial culture

The monoclonal bacteria (*Escherichia coli* (*E. coli*, ATCC25922), *Staphylococcus aureus* (*S. aureus*, ATCC2923)) on the Luria–Bertani (LB) solid medium was transferred to a 5 mL LB liquid medium and cultured at 37 °C at 200 rpm for 8 h to reach the logarithmic growth period.

2.8. The dose-dependent antibacterial ability of H_2O_2

E. coli (1.0×10^8 CFU mL^{-1}, colony-forming units, CFUs) were incubated separately with HAc/NaAc buffer and different concentrations of H_2O_2 (1.0×10^{-6}, 1.0×10^{-5}, 1.0×10^{-4}, 1.0×10^{-3}, 1.0×10^{-2} and 1.0×10^{-1} M) for 30 min. Then 100 μL of diluted bacteria were coated on agar culture plates to culture at 37 °C for another 18 h.

2.9. In vitro antibacterial assays

The plate counting method was used to determine the antibacterial performance of H_2O_2 through counting the number of CFUs. The experiments were accomplished in HAc/NaAc buffer. Typically, experiments for *E. coli* were divided into eight groups: (1) bacteria, (2) bacteria + Fe-CDs, (3) bacteria + H_2O_2, (4) bacteria + Fe-CDs + H_2O_2, (5) bacteria + NIR, (6) bacteria + Fe-CDs + NIR, (7) bacteria + H_2O_2 + NIR, and (8) bacteria + Fe-CDs + H_2O_2 + NIR. Each group contained the same number of bacteria. The final working concentrations were 200 μg mL^{-1} and 1 mM for Fe-CDs and H_2O_2, respectively. The mixtures were incubated in a 37 °C shaker with a shaking speed of 200 rpm for 30 min. The mixtures with NIR exposure were first cultivated for 25 min and then exposed to the NIR laser irradiation for 5 min (808 nm, 2 W cm^{-2}). Subsequently, 100 μL of the diluted mixtures were coated on agar plates and cultured at 37 °C for 18 h. Finally, relative bacterial activity was obtained from counting the numbers of colonies. For *S. aureus*, the experimental procedures were carried out using the same method.

$$\text{Antibacterial ratio}\% = \left(1 - \frac{\text{CFU}_{(\text{each group})}}{\text{CFU}_{(\text{control})}}\right) \times 100\%$$

Where CFU (control) is the CFUs of control group, and CFU (each group) is the CFUs of the groups with different treatments as mentioned above.

2.10. In vitro biofilm disruption

80 μL *S. aureus* or *E. coli* (1.0×10^7 CFU mL^{-1}) and 720 μL LB liquid medium were added into 24-well microtiter plates and cultured at 37 °C for 60 h. After that, the plate was immersed with PBS. The obtained biofilms were treated with PBS, Fe-CDs, H_2O_2, Fe-CDs + H_2O_2, NIR, Fe-CDs + NIR, H_2O_2+ NIR, and Fe-CDs + H_2O_2 + NIR (808 nm, 2 W cm^{-2}, 5 min), respectively. The final working concentrations were 200 μg mL^{-1} and 1 mM for Fe-CDs and H_2O_2, respectively. The mixtures were incubated in a 37 °C for 30 min and abandon the supernatant. Then, 200 μL crystal violet (CV) dye was added at room temperature for 15 min. After the well were washed with PBS to remove the free crystal violet dye, the plate was placed upside down blotting paper to dry. 200 μL DMSO was added to remove the fixed crystal violet dye. After 2 h, the eluant absorbance at 590 nm was detected.

2.11. Live/dead fluorescent staining

The groups were divided as the in vitro antibacterial experiment. Afterward, the samples were vibrated and incubated for 2 h at room temperature. Then the samples were incubated with SYTO-9 and PI for 30 min in the dark, respectively. In the following, the stained bacterial cells were visualized with confocal laser microscopy (CLSM).

2.12. Intracellular ROS measurement

The DCFH-DA was applied to determine the intracellular ROS levels. To begin with, after cultivation for an overnight of *E. coli*, we divided it into 8 groups as the in vitro antibacterial experiment and added Fe-CDs to group (2), (4), (6), (8) to incubate for 2 h. Then, all samples were incubated with 1 mL of DCFH-DA (10 μM) for 30 min in the dark and then washed by phosphate-buffered saline (PBS). After the introduction of H_2O_2 and NIR, the intracellular ROS level was observed by CLSM.

2.13. Morphological characterization of bacteria

After different treatments, the mixtures were centrifuged (6000 rpm) for 5 min, washed twice with PBS, and fixed by 4% paraformaldehyde for 2 h. Subsequently, the bacteria were gradually dehydrated using 50%, 70%, 90%, and 100% ethanol. Finally, SEM was used to observe the morphology changes of all the samples.

2.14. Cellular experiments

The mouse embryonic fibroblast cell line (NIH-3T3) was purchased from Beijing Vital River Laboratory Animal Technology Co., Ltd. NIH-3T3 cells were cultured in DMEM media. The cell lines were incubated in an incubator at 37 °C containing 5% CO_2.

NIH-3T3 cells suspension with a concentration of 5×10^3 cells per well were seeded in 96-well plates and incubated for 24 h. Subsequently, the medium was abandoned and different concentrations of Fe-CDs (0, 12.5, 25, 50, 100, 200 μg mL^{-1}) dispersed in DMEM were added into 96-well plates with NIH-3T3 cells. After incubated for another 24 h, the MTT assay was used to determine the cytotoxicity according to a standard protocol. The same procedure was used to determine the proliferation effect of Fe-CDs (200 μg mL^{-1}, using concentration) toward NIH-3T3, except that NIH-3T3 cells suspension were seeded in 96-well plates with a concentration of 2×10^3 cells per well and incubated for 1 d, 3 d, and 5 d, respectively.

2.15. Animal use and care

BALB/c female mice (6 weeks, 15–18 g) were purchased from Vital River Laboratories (Beijing, China). All animal care and experimental procedures were under institutional policies for animal health and well-being, and were approved by the Institutional Animal Care and Use Committee (IACUC) of the Academy of Military Medical Science (AMMS, Beijing, China) (IACUC-DWZX- 2021–046).

2.16. In vivo antibacterial and wound-healing evaluation

A rounded wound approximately 6 mm in diameter was established on the dorsum of each mouse. Then, the infected wound model was constructed after injecting 10 μL suspension (2.0×10^8 CFU mL^{-1}) into the wound. After 24 h, the mice were divided randomly into five groups: (1) control group (HAc/NaAc buffer), (2) H_2O_2 group, (3) Fe-CDs + H_2O_2 group, (4) Fe-CDs + NIR group, and (5) Fe-CDs + H_2O_2 + NIR group. The treatments were applied on day 0 and 4. For the groups with NIR exposure, which was directly irradiated to the wound, the temperature changes on the wound bed were recorded by an infrared thermal imaging camera (FLIR, E40). Meanwhile, photographs of the wound bad were taken on day 0, 2, 5, 7, and 10 and the size of the wound

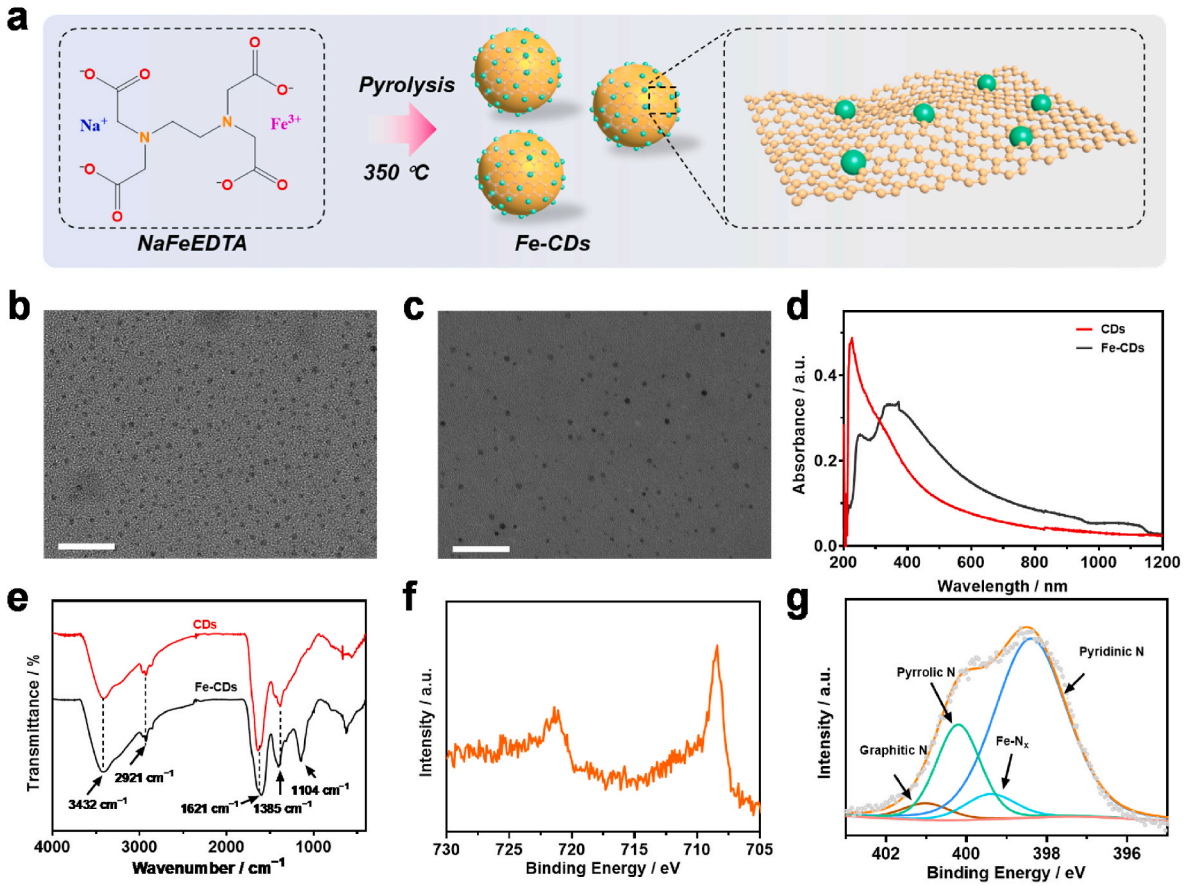

Fig. 1. Synthesis and structure characterization of Fe-CDs and CDs. a) Schematic illustration of the synthesis process of Fe-CDs. TEM images of b) Fe-CDs and c) CDs. d) UV–Vis–NIR absorption spectra of Fe-CDs and CDs. e) FT-IR spectra of Fe-CDs and CDs. High-resolution XPS spectra of f) Fe 2p and g) N1s of Fe-CDs. Scale bar: 50 nm.

was measured following: Size $= \pi\left(\frac{d}{2}\right)^2$, where d was the average diameter of wound. The body weight of mice was also measured. The mice were sacrificed after 10 days and the primary organs and granulation tissues over the wound bed were harvested, fixed in 4% paraformaldehyde overnight, followed by dehydration, and then embedded in paraffin for pathological histology, immunohistochemistry, and immunofluorescence staining analysis.

2.17. Histology, immunohistochemistry, and immunofluorescence staining

The primary organs and granulation tissues were sliced on the paraffin slicer. The slices, 4 μm in thickness, were prepared and followed by dewaxing. Serially sections were used for hematoxylin-eosin staining and the sections of granulation tissue were also used for immunohistochemical staining with IL-6, TNF-α, VEGF, IL-10 and TGF-β. To evaluate neovascularization, sections were used to incubate with the primary antibodies CD31 (Servicebio, GB13044) and α-SMA (Servicebio, GB13428) overnight at 4 °C. Afterward, sections were washed three times with PBS (pH = 7.4) in a Rocker device for 5 min and incubated with secondary antibodies at room temperature for 50 min in dark condition, and were washed three times with PBS (pH = 7.4) for 5 min and incubated with 4', 6-diamidino-2-phenylindole (DAPI) solution to label nucleus. For collagen deposition evaluation, the primary antibodies were vimentin (Servicebio, GB11192) and collagen (Servicebio, GB12021).

2.18. Statistical analysis

All experiments were repeated at least 3 times and presented as mean ± SD. Statistical significance was calculated using unpaired Student's two-sided *t*-test, and statistically significant differences are shown with $^{*}p < 0.05$, $^{**}p < 0.01$, $^{***}p < 0.001$ and ns: no significant.

3. Results and discussion

3.1. Synthesis and structure characterization of Fe-CDs and CDs

Fe-CDs were fabricated through pyrolysis of NaFeEDTA at 350 °C for 2 h and then dialyzed for 2 days (Fig. 1a), as EDTA, with a flexible structure, is a common starting material for CDs and a saturated schiff-base-like structure could be formed after EDTA chelated with metal ions [23]. Transmission electron microscope (TEM) was used to characterize the morphology and size distribution of the obtained Fe-CDs (Fig. 1b). Lateral sizes ranged from 1.3 nm to 3.5 nm were observed (Fig. S1a). Meanwhile, using $Na_2[H_2(EDTA)]\cdot 2H_2O$ as precursor, pristine CDs were also synthesized by the same method, which exhibited a similar morphology with that of Fe-CDs (Figs. 1c and S1b). The high-resolution TEM (HR-TEM) image of Fe-CDs, as well as CDs, exhibited a lattice spacing of 0.24 nm, corresponding to (100) interplanar spacing of graphite carbon (Figs. S1c and S1d) [18,24] Compared to CDs, the powder X-ray diffraction patterns of Fe-CDs showed a higher angel peak (≈25°→≈26°) (graphite carbon), indicating the Fe doped to the carbon framework resulted in the higher disordered graphite-like structure. And there was another weak peak at about 36° for Fe-CDs, which was attributed to FeN phase (Fig. S2) [25].

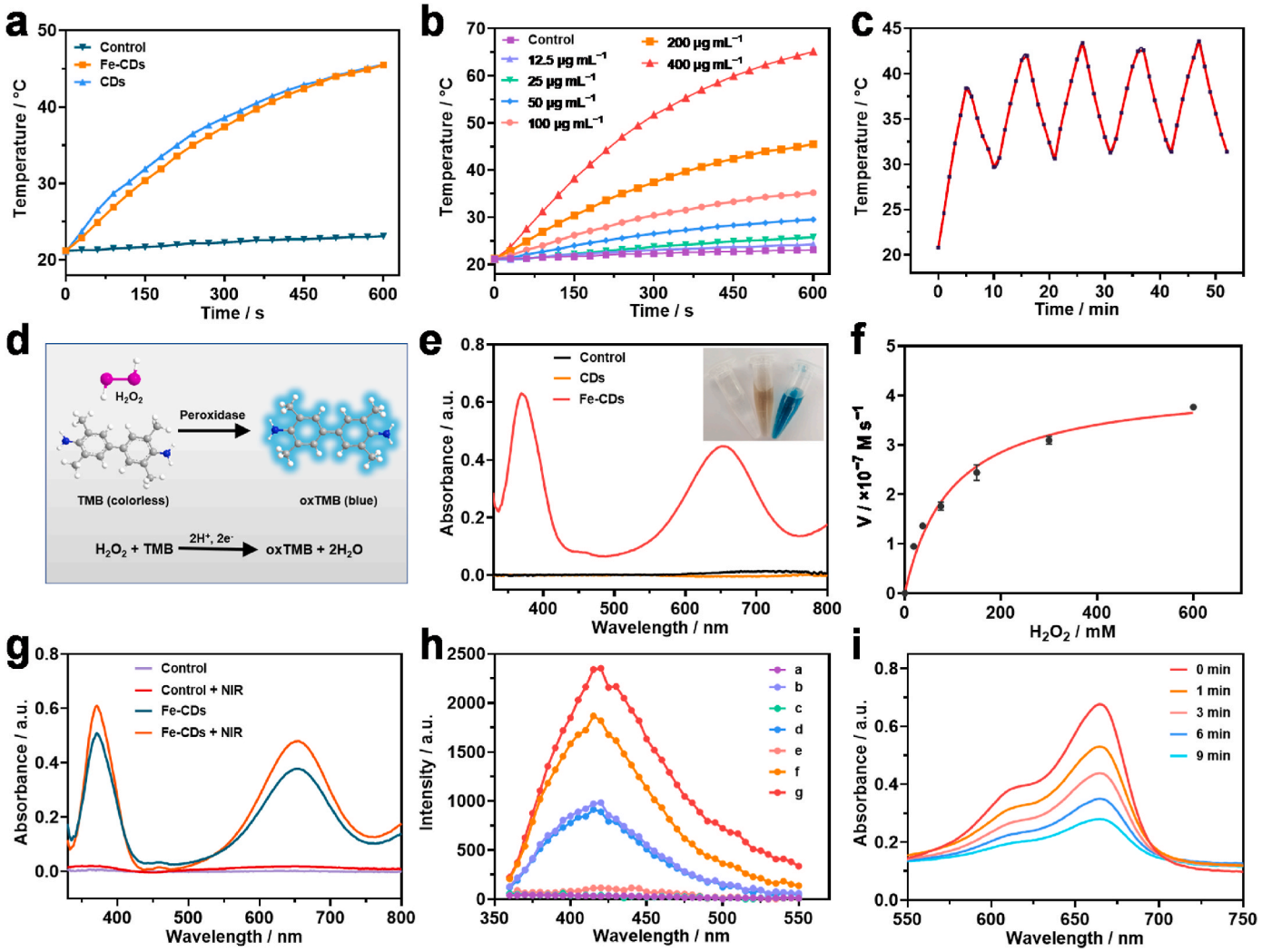

Fig. 2. Characterization of photothermal and peroxidase-like activity of Fe-CDs and CDs. a) Temperature elevation of control (pure water), CDs and Fe-CDs aqueous dispersions (1.0 mL) under NIR laser irradiation (808 nm, 2 W cm^{-2}), and b) Fe-CDs aqueous dispersions (1.0 mL) with different concentrations. c) Real-time temperature measurement of Fe-CDs under NIR laser irradiation (808 nm, 2 W cm^{-2}) for 5 cycles. d) Schematic illustration of the oxidation reaction of TMB. e) Absorbance of oxTMB in the control (TMB single-component substrate solution), CDs, and Fe-CDs groups, the inset is the corresponding visual color changes. f) Steady-state kinetic assay of Fe-CDs for H_2O_2 substrate. g) Increased absorbance of oxTMB after exposure to NIR laser irradiation (808 nm, 2 W cm^{-2}). h) Fluorescence spectra of the (a) TA; (b) Fe-CDs; (c) H_2O_2; (d) Fe-CDs + TA; (e) H_2O_2 + TA; (f) Fe-CDs + H_2O_2 + TA; (g) Fe-CDs + H_2O_2 + TA + NIR. i) Time-dependent degradation of MB after adding Fe-CDs and H_2O_2 under NIR laser irradiation (808 nm, 2 W cm^{-2}).

Spectral analyses were carried out to further characterize Fe-CDs and CDs. A broad absorption of CDs and Fe-CDs was observed from the ultraviolet–visible–NIR (UV–Vis–NIR) absorption spectrum (Fig. 1d). The absorption peaks at about 240 and 370 nm were ascribed to the π–π* transition of the conjugated C=C structure and the n–π* transition of the C=O structure, respectively. The existence of the oxygen and nitrogen-containing functional groups would narrow the energy levels of valence electron transition and result in the strong NIR absorption, implying that CDs and Fe-CDs could be used as photothermal agents [26]. Compared to CDs, the absorption intensity for Fe-CDs from the visible region to the NIR region was increased, which was due to metal-to-graphite charge-transfer transitions [27]. Fig. 1e represented the Fourier transform infrared (FT-IR) spectra of CDs and Fe-CDs. The peaks at around 3432, 2921, 1621, and 1385 cm^{-1} were assigned to the O–H, $–CH_2–$ antisymmetric, C=O/C=N, and C–N stretching vibrations, respectively. The broad absorption from 3200 to 3400 cm^{-1} implied the presence of hydroxy (−OH), and amino ($-NH_2$) groups on the samples [28]. Notably, there was a newly apparent peak in the FT-IR spectra of Fe-CDs at approximately 1104 cm^{-1}, arising from the stretching vibration of the metal-ligand bond [29]. In addition, the peak resulted from C=O/C=N exhibited a blue-shift after Fe doping since Fe was chelated with N or O. Thus, the results of FT-IR demonstrated the coordination between Fe and CDs. The Fe 2p X-ray photoelectron spectroscopy (XPS) spectrum of Fe-CDs was shown in Fig. 1f, further verifying the existence of Fe. For the XPS spectra of N 1s, it could be observed a new peak of about 399.4 eV, which was assigned to Fe-N_x (Fig. 1g) [30]. The high-resolution XPS spectra of N 1s and O 1s displayed different amount in species for CDs and Fe-CDs, suggesting that Fe doping induced the changes of local chemical environment of N and O elements of CDs (Figs. S3 and S4, Tables S1 and S2). Inductively coupled plasma mass spectrometry (ICP-MS) determined that the Fe content in the synthesized Fe-CDs was 1.31 wt%. The zeta potential of CDs was approximately neutral (Fig. S5). Compared to CDs, probably owing to the different proportion of hydrophilic groups such as decreasing amount of amino groups and increasing amount of carboxyl groups on the surface of Fe-CDs, the zeta potential of Fe-CDs was more negative. The Raman spectra of Fe-CDs and CDs were presented in Fig. S6, from which we could see both contained a peak at 1340 cm^{-1} named D band and a peak at 1570 cm^{-1} named G band. The calculated I_D/I_G intensity values of Fe-CDs and pristine CDs were 0.99 and 1.01, respectively, indicating

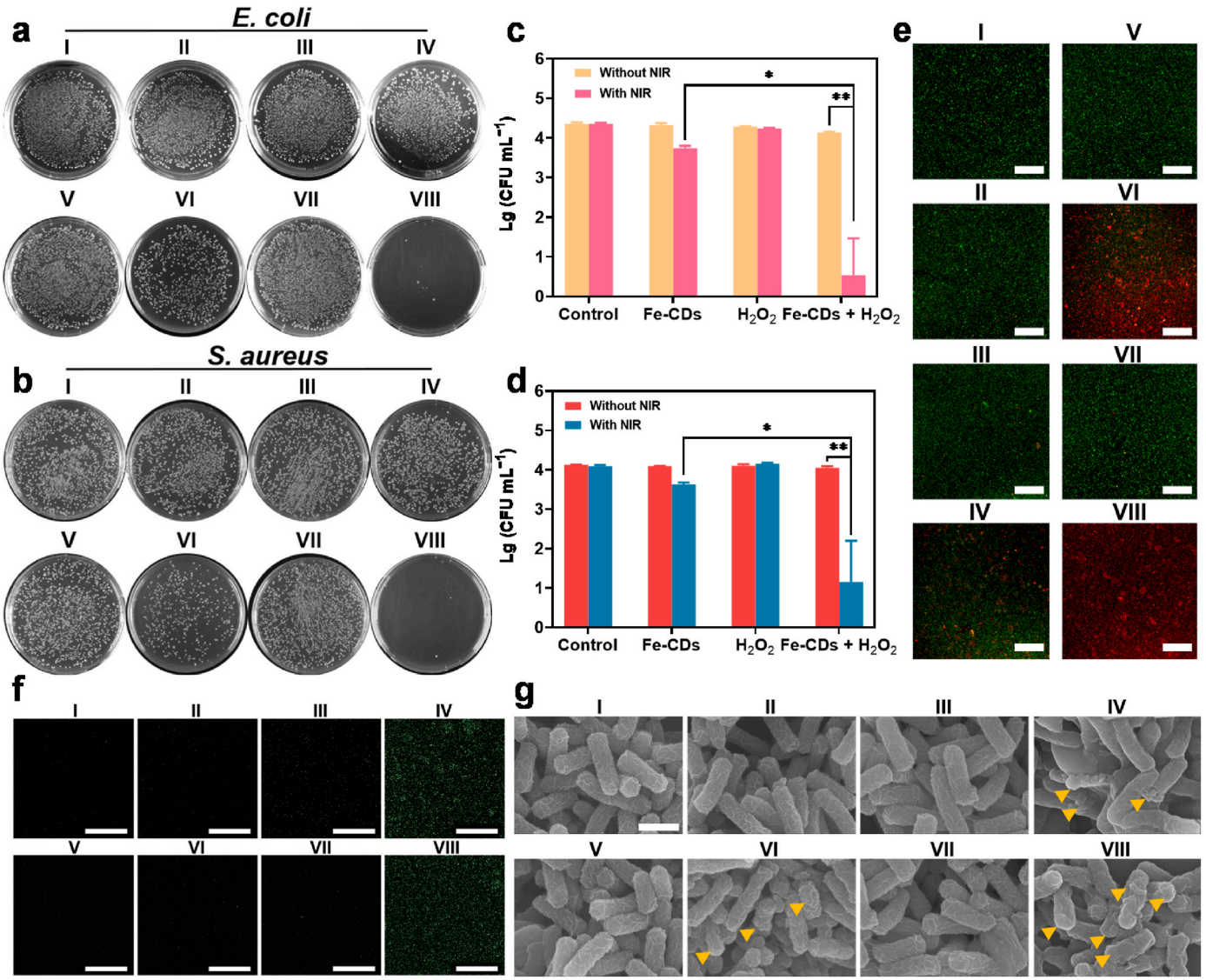

Fig. 3. In vitro antibacterial performance of Fe-CDs. Agar plate digital photographs of bacterial colonies of a) *E. coli* and b) *S. aureus* with different treatments. Corresponding bacterial viability measurement of c) *E. coli* and d) *S. aureus* with different treatments. e) Representative CLSM images for a Live/Dead bacterial viability assay of *E. coli* with different treatments. Scale bar: 200 μm. f) Fluorescence images of *E. coli* with different treatments showing the production of ROS. Scale bar: 100 μm. g) SEM images of *E. coli* with different treatments. Yellow arrows represent the typical distortion of bacterial morphology. Scale bar: 1 μm. (I) Control (HAc/NaAc buffer); (II) Fe-CDs; (III) H_2O_2; (IV) Fe-CDs + H_2O_2; (V) NIR; (VI) Fe-CDs + NIR; (VII) H_2O_2 + NIR; (VIII) Fe-CDs + H_2O_2 + NIR. (*$p < 0.05$ and **$p < 0.01$).

that these two samples possessed carbon defects and graphitic structure [31]. The defects combined with the Fe doping would lead to high stable and high-density distribution of active sites, contributing to the catalytic efficiency [32]. The obtainment and analysis of the morphology and chemical structure data strongly indicated that we successfully achieved the synthesis of Fe-CDs and CDs, and it is conceivable that Fe doping advanced the structure of CDs.

3.2. Photothermal and peroxidase-like activity of Fe-CDs

Encouraged by the strong absorption at the NIR region, the photothermal behavior of Fe-CDs was investigated through recording temperature increase and calculating the photothermal conversion efficiency. The temperature of Fe-CDs and CDs aqueous dispersions at the same concentration increased to about 45.5 °C within 10 min, while the pure water showed negligible temperature variation (Fig. 2a). It showed that Fe-CDs remained a similar photothermal effect to CDs. Furthermore, a concentration-dependent temperature increase of Fe-CDs was demonstrated, as shown in Fig. 2b. The photothermal conversion efficiency of Fe-CDs was calculated to be 35.11%, indicating that Fe-CDs could effectively convert light to heat. (Fig. S7). Meanwhile, it was also verified that Fe-CDs showed excellent photostability after being subjected to laser on-off cycles (Fig. 2c).

Subsequently, the POD-mimic activities of Fe-CDs and CDs were evaluated. It was previously reported that the colorless 3,3′,5,5′-tetramethylbenzidine (TMB) could be catalyzed to the blueness oxidized TMB (oxTMB) in the presence of H_2O_2 and POD-like mimics (Fig. 2d) [33,34]. Accordingly, the POD-like activities of Fe-CDs and CDs toward TMB were determined firstly. Both the control group and CDs group displayed negligible absorbance. However, with the addition of Fe-CDs, the color of the sample changes obviously with time-varying, indicating that Fe-CDs can effectively catalyze the oxidation of TMB (Figs. 2e and

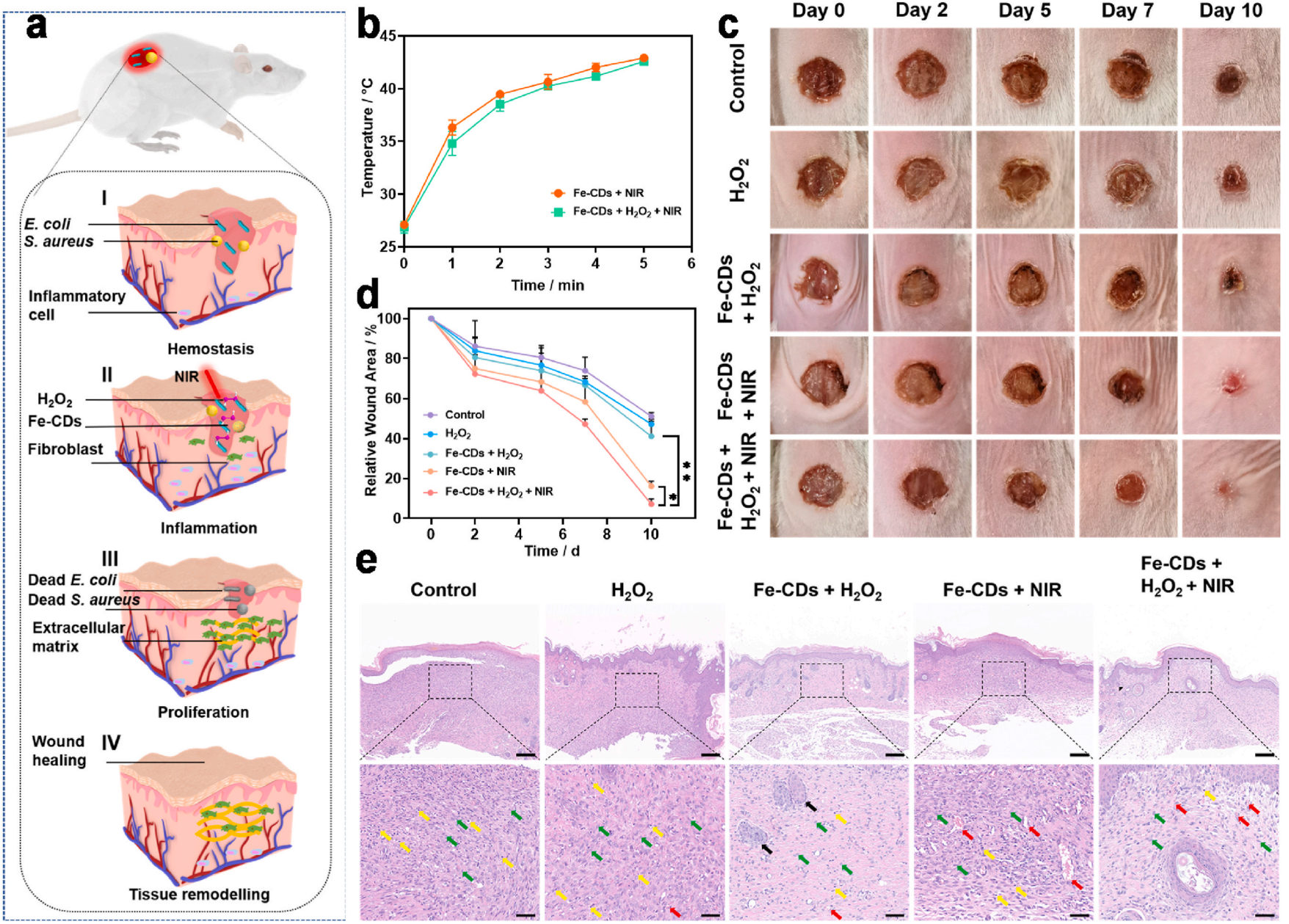

Fig. 4. Wound disinfection and healing efficacy of Fe-CDs. a) Schematic illustration of the application of Fe-CDs-based therapeutic platform toward wound healing. b) Temperature evolution on BALB/c mice back wounds with injecting Fe-CDs during NIR laser irradiation (808 nm, 2 W cm^{-2}, 5 min). c) Representative macroscopic appearance of *E. coli*-infected wounds treated with HAc/NaAc buffer, H_2O_2, Fe-CDs + H_2O_2, Fe-CDs + NIR, and Fe-CDs + H_2O_2 + NIR ($n = 3$). d) Relative mean wound area of *E. coli*-infected mice at 10 days post treatment. e) Representative photos of H&E staining of dermal wounds. Yellow arrows represent inflammatory cells, including lymphocytes, neutrophils, and macrophages; black arrows reflect hair follicles; green arrows indicate fibroblasts; and red arrows stand for new blood vessels. Scale bar: 200 μm. The scale bars for the magnified images are 50 μm. (*$p < 0.05$, and **$p < 0.01$).

S8). These results showed that Fe doping endows CDs the ability to carry out the POD-like catalytic reaction, which was highly correlated with the Fe–N coordination [35]. Furthermore, the steady-state kinetic assay was carried out to systematically analyze the catalytic activity of Fe-CDs. Upon the addition of a series of concentrations of H_2O_2 into TMB in the presence of Fe-CDs, a nature of H_2O_2 concentration-dependent absorbance was obtained (Fig. 2f). TMB concentration-dependent absorbance was also achieved using the same method (Fig. S9). Thereafter, according to the Beer-Lambert law, the initial reaction rates were figured out, and then, the maximum initial velocity (V_{max}) and the Michaelis–Menten constant (K_m) were obtained by using the Lineweaver–Burk plot. The K_m value of Fe-CDs was determined as 97.64 mM for H_2O_2 or 0.348 mM for TMB (Table S3), which was comparable to that of the well-studied Fe_3O_4 nanozyme or the natural horseradish peroxidase (HPR) [3]. Remarkably, the characteristic absorption peaks of oxTMB at about 370 and 652 nm were enhanced after being exposed to the NIR laser irradiation (Fig. 2g), which was owing to the increased electron transfer efficiency resulting from the mild photothermal effect [36]. To determine the catalytic mechanism of Fe-CDs, the generation of •OH was verified through fluorescence assay, which was due to the production of fluorescent product 2-hydroxyterephthalic after •OH reacted with terephthalic acid (TA) (Fig. S10). A significant fluorescence change was shown in the Fe-CDs + H_2O_2 + TA group, and the change was enhanced with NIR irradiation, indicating the production of •OH and the photoenhanced effect (Fig. 2h). The generation ability of •OH was also demonstrated by a chemical probe methylene blue (MB). After adding Fe-CDs and H_2O_2 (±NIR), a gradually decreased MB-characteristic absorption peak was observed, and the normalized absorbance of MB (A/A_0) at 665 nm was calculated (Figs. 2i and S11). There was a higher decreased MB for the group with NIR laser irradiation, which was good consistent with the result in the TMB and TA assays. These results showed that Fe-CDs were able to act as POD mimic with highly photoenhanced catalytic activity. Overall, the excellent enzyme-like activity and photothermal effect enabled Fe-CDs to act as promising antibiotics-free nanomaterials for wound disinfection and healing.

3.3. In vitro antibacterial performance of Fe-CDs

As bacterial infection is the overriding challenge for wound healing, H_2O_2, one kind of ROS, is extensively used for bacterial disinfection. Thus, we firstly assessed the antibacterial performance of H_2O_2 at various concentrations, which showed that at least 0.3% (≈0.1 M) was necessary to reach an excellent antibacterial performance (Fig. S12). However, such high concentrations of H_2O_2 would delay the efficiency of wound healing [37]. Therefore, it was more suitable and effective to convert H_2O_2 at a low level into •OH since, compared to H_2O_2, •OH as highly active ROS had higher oxidizing activity and could induce a more severe oxidative damage to bacteria [38]. The plate counting experiments were carried out to test the antibacterial activity of Fe-CDs against *S. aureus* and *E. coli* (Fig. 3a and b). As shown in Fig. 3c and d, H_2O_2 (0.003%, 1 mM) with the catalytic effect of Fe-CDs could cause an obvious reduction in the viability of *E. coli* (about 40%) and *S. aureus* (about 16%) while *E. coli* or *S. aureus* treated alone with H_2O_2 or Fe-CDs showed a scarcely decrease in the bacterial viability. These phenomena could be attributed to the production of •OH. Remarkably, the bactericidal rate in the Fe-CDs + H_2O_2 + NIR group was 99.68% for *S. aureus* or 99.85% for *E. coli*, and much more effective than the Fe-CDs + NIR group (68.59% for *S. aureus* or 75.95% for *E. coli*). This demonstrated the synergy of •OH plus local mild heat could actively attack bacteria than mild heat alone. We also performed Live/Dead assays for *E. coli* by using fluorescent dye SYTO-9 and PI, which showed similar bactericidal results through confocal laser scanning microscope (CLSM) (Fig. 3e).

To determine the antibacterial mechanism of the Fe-CDs-based therapeutic platform, the ROS production was confirmed by incubating with fluorescent probe 2′,7′-dichlorofluorescein diacetate (DCFH-DA) (Fig. 3f). There was higher fluorescence intensity in the Fe-CDs + H_2O_2 group and Fe-CDs + H_2O_2 + NIR group, indicating a higher-level production of ROS. To further investigate the antibacterial mechanism, scanning electron microscope (SEM) was used to observe the bacterial morphology and the bacterial membrane integrity (Figs. 3g and S13). From the SEM images, the morphology of both *S. aureus* and *E. coli* in the control and H_2O_2 groups (±NIR) remained intact and original appearance. In the Fe-CDs group, the bacteria-nanocatalyst adhesion was observed, which was more clearly in the TEM images. (Fig. S14). Partial wrinkling and disruption of bacterial membrane could be observed in the Fe-CDs + H_2O_2 group and Fe-CDs + NIR group. In the Fe-CDs + H_2O_2 + NIR group, the structure of bacteria was significantly destroyed and no longer kept the globular or rod shape. Thereby, the full antibacterial performance of Fe-CDs was dependent on the addition of H_2O_2 plus NIR laser. The lethal •OH and the local mild heat are the major and synergistic inducements for the antibacterial effect. In summary, the above results indicated that Fe-CDs could adhere onto the bacterial surface and, in the presence of H_2O_2 or NIR laser, induce the ROS- and heat-dependent bacterial killing, manifesting as a typical membrane rupture-death fate [39]. Based on the proposed mechanism, we then also investigated the potential of Fe-CDs-based therapeutic platform for eradicating biofilm since biofilm was the main factors that cause antibiotic resistance and delay wound healing [40]. With the crystal violet-based colorimetric assay (CV), the quality of the biofilms was quantified. As shown in Fig. S15, both the treatment of Fe-CDs + H_2O_2 and Fe-CDs + NIR showed certain effect to biofilm disruption. Moreover, upon the addition of Fe-CDs, H_2O_2 and NIR, biofilm disruption was the most obvious, which was in consistent with the antibacterial results.

3.4. Wound disinfection and healing efficacy of Fe-CDs

Motivated by the outstanding in vitro antibacterial performance of Fe-CDs, the effect of Fe-CDs in wound disinfection and healing was evaluated using bacterial-infected cutaneous wound model. Before that, we investigated the cytotoxicity of Fe-CDs on NIH-3T3 cells (Fig. S16). It could be seen that the cell viability was in the normal range even at the dose of 200 μg mL^{-1}, which demonstrated the good biocompatibility of Fe-CDs. The schematic diagram in Fig. 4a illustrated the application of Fe-CDs-based therapeutic platform to wound healing, which usually takes place in a temporal sequence but also overlapped stages, namely hemostasis, inflammation, proliferation, and tissue remodeling [41]. First of all, a round wound about 6 mm in diameter was established by nicking wounds on the back of each female BALB/c mouse, and then, the infected wound model was constructed after dropping 10 μL E. *coli* (or *S. aureus*) suspensions with a cell density of 2.0×10^8 (or 1.0×10^7) CFU mL^{-1}. After the bacterial infection was sustained for 24 h, the mice were randomly divided into five groups and implemented on day 0 and 4 for the following treatments: (1) Control (HAc/NaAc buffer), (2) H_2O_2, (3) Fe-CDs + H_2O_2, (4) Fe-CDs + NIR and (5) Fe-CDs + H_2O_2 + NIR. The concentration of Fe-CDs was consistent in group (3), (4), and (5). After exposure to the NIR laser irradiation, an ascending temperature in the mice wound bed of Fe-CDs + NIR group and Fe-CDs + H_2O_2 + NIR group was recorded. As shown in Figs. S17 and 4b, the highest temperature in the wound area was controlled to be less than 45 °C, which was in the range of mild temperature (41–45 °C) that can reduce inflammation response and thermal damage to normal tissues but remained the antibacterial effect and was able to enhance the catalytic activity of Fe-CDs [42,43]. The traumas area was photographed and calculated. Fig. 4c presented the trends of *E. coli*-infected continuous wound closure and escharosis variation in different groups. In the control group and H_2O_2 group, obvious bacterial deposits and the development of suppuration could be seen during the whole course, illustrating the dilemma of relying solely on the immune system to clear bacteria. Furthermore, the long-time of eliminating bacterial would discourage the upcoming wound closure. Notably, the wounds of the Fe-CDs + H_2O_2 + NIR group completely healed after 10 days whereas other groups including the

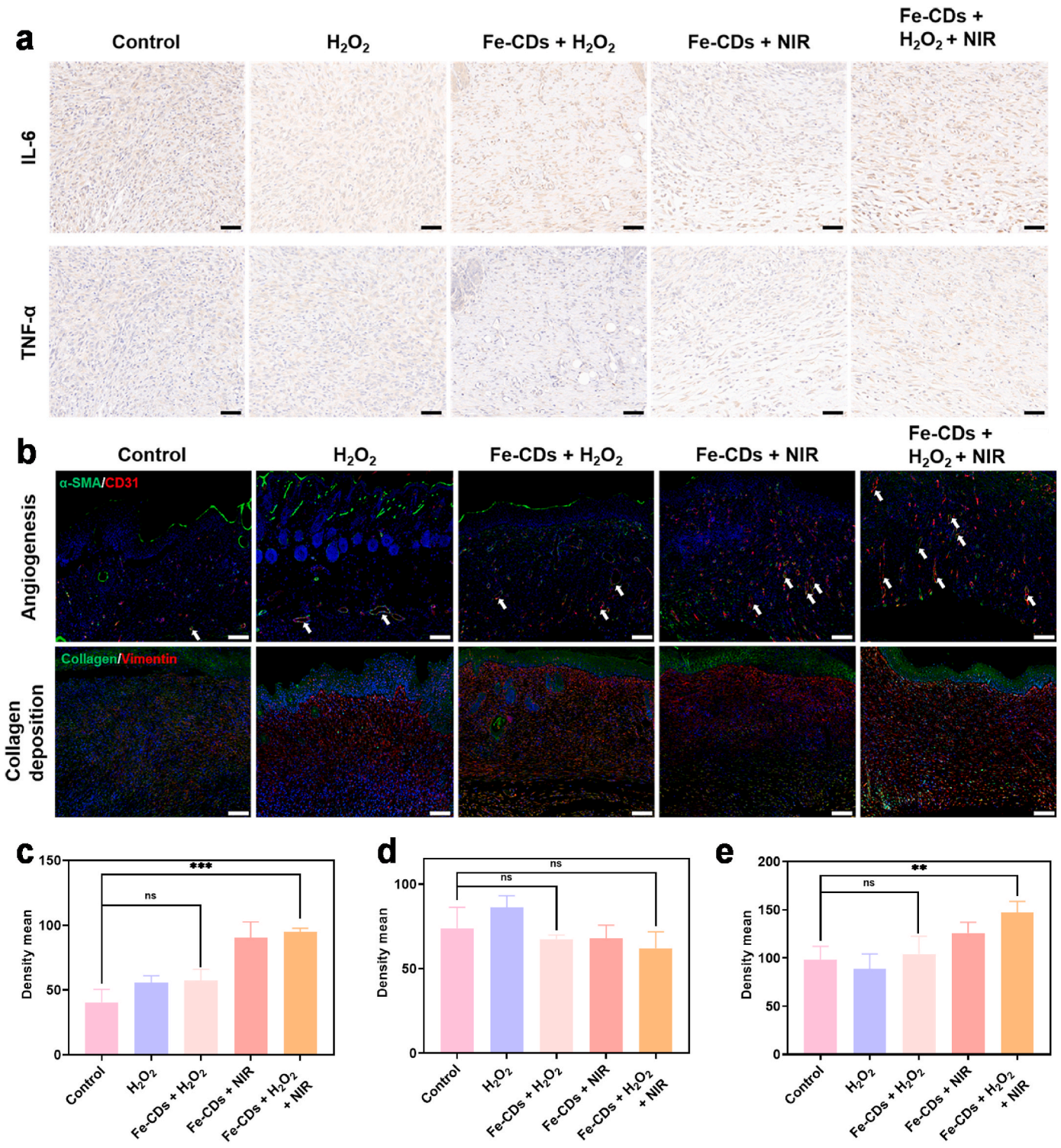

Fig. 5. Intrinsic drive for Fe-CDs-mediated wound healing. a) Micrographs of immunohistochemical staining of IL-6 and TNF-α in granulation tissues on day 10. Scale bar: 50 μm. b) Double immunofluorescence staining of α-SMA (green) and CD31 (red), collagen (green) and vimentin (red). Scale bar: 100 μm. c) Quantification of the CD31 labeled structures. d) Quantification of vimentin. e) Quantification of collagen. (**$p < 0.01$, ***$p < 0.001$, and ns: no significant).

Fe-CDs + H_2O_2 group and Fe-CDs + NIR group showed unhealed wounds, which was due to the synergistic effect of ROS plus local mild heat (Fig. 4d).

Furthermore, the dermal tissues around the original bacterial infected-wounds of respective groups on day 10 were collected and pathologically analyzed to investigate the microscopic changes of the wound healing process. From the hematoxylin and eosin (H&E) staining images (Fig. 4e), new epidermis could be seen in the damaged area, and the dermis was repaired by large amounts of connective tissue. Abundant fibroblasts (marked by green arrows) were also observed. Tissue in the control group and H_2O_2 group exhibited many incomplete epidermal layers and disordered collagen fibrils. Meanwhile, many lymphocytes and neutrophils (marked by yellow arrows) can be observed, indicating severe wound infection. In contrast, H&E images of Fe-CDs + H_2O_2 +

NIR group showed intact epidermal layers and regular collagen fibrils with regenerated follicles (marked by black arrows) and neovascularization (marked by red arrows), displaying better antibacterial efficiency and wound healing relative to the other groups. Similar results for the *S. aureus*-infected wound model were also observed in Fig. S18. These results demonstrated the striking promoting wound healing effect of the Fe-CDs-based therapeutic platform. Besides, the major organs, including the heart, liver, spleen, lung, and kidney, from the treated mice were gained for H&E staining, and no substantial inflammatory or pathological damages were observed (Figs. S19 and S20). The body weight of each mouse was recorded, and there was no statistically significant difference between the five groups (Figs. S18c and S21).

3.5. Intrinsic drive for Fe-CDs-mediated wound healing

To further explore the inherent imputes of the wound healing process, immunohistochemistry and double immunofluorescence staining experiments were carried out. Since the inflammatory response due to the wound infection was one of the main reasons inhibiting wound healing, the expression of the two typical proinflammatory factors, namely interleukin-6 (IL-6), and tumor necrosis factor-α (TNF-α), were evaluated by immunohistochemistry to determine the infection-preventing efficiency of Fe-CDs (Fig. 4f). A large amount of the above two typical proinflammatory factors were detected in the control group and H_2O_2 group. In contrast, the Fe-CDs + H_2O_2 + NIR group showed the lowest expression of proinflammatory factors, implying few infections formation. Moreover, Interleukin-10 (IL-10), a potent anti-inflammatory cytokine, and transforming growth factor-β (TGF-β) [44], an important cellular mediator for wound healing were also determined using the immunohistochemistry method (Fig. S22). High secretion was observed in the Fe-CDs + H_2O_2 + NIR group, further indicating low inflammatory response and the preventing infection ability of Fe-CDs-based therapeutic platform. The production of ROS and local heat assumed the primary responsibility for this phenomenon.

In addition to preventing infection, the Fe-CDs-based therapeutic platform also showed an advantage in wound repair. The expression of vascular endothelial growth factor (VEGF) was determined using the immunohistochemistry method (Fig. S23), since VEGF, secreted from the inducement of macrophages during the end of the inflammation stage, plays an important part in the neovascularization of cutaneous wound healing [41]. An up-regulated secretion of VEGF was observed in the Fe-CDs + H_2O_2 + NIR group relative to the control group, which would contribute to angiogenesis and tissue remodeling. MTT assay was applied to detect the proliferation effect of Fe-CDs to fibroblast. As shown in Fig. S24, the optical density of fibroblasts for Fe-CDs was significantly increased, which was probably due to Fe from Fe-CDs was closely related to cell proliferation and other functions as a vital trace element in the human body [45]. Fibroblasts would synthesize and secrete plenty of collagen fibers, increase the deposition of extracellular matrix (ECM) such as collagen, and promote the emergence of granulation tissue to fill the defects of wound tissue together with new capillaries in the proliferation stage [46]. In addition, mild temperature caused by NIR laser irradiation would induce heat shock response (HSR) with a coordinated expression of growth factors, which included TGF-β playing an important part in the inflammatory response and fibroblast proliferation [47].

Furthermore, double immunofluorescence staining of neovascularization and collagen was conducted to determine angiogenesis and collagen deposition, respectively (Figs. 5b and S25). As the microscope observation of α-smooth muscle actin positive cells (α-SMA) and CD31 staining displayed, CD31 structures (red) were closely connected with α-SMA (green), which meant vascular ducts (marked by white arrows). The wound vascular density in the Fe-CDs + NIR group and Fe-CDs + H_2O_2 + NIR group was significantly higher than other groups, which allowed for the delivery of nutrients and maintenance of oxygen homeostasis, and thereby promoted the cell proliferation and tissue regeneration (Fig. 5c). From the microscope observation of collagen and vimentin staining, it could be seen that all of the groups showed approximately positive vimentin (red) expression (Fig. 5d). It also displayed that collagen (green) was distributed around vimentin, which suggested that vimentin mainly represented fibroblasts who are capable to secrete collagen. Combined with the data in Fig. 4c, the above results reflected that the mice of the five groups were probably at different stages of wound healing. Compared to the control group, the Fe-CDs + H_2O_2 + NIR group displayed much more collagen deposition with higher levels of orientation (Fig. 5e) The proliferation of fibroblast and directional alignment of collagen fibers contributed to the deposition of ECM, providing a physical scaffold for the cellular activity characteristic of contracting the smooth muscle for wound repair. In summary, these results denoted that the Fe-CDs-mediated therapeutic platform was potent to promote angiogenesis and collagen deposition.

4. Conclusion

In summary, we develop an appealing paradigm of PTT-aided ROS-producing POD-mimic for antibacterial therapy and wound healing in a highly efficient and safe manner. The as-prepared Fe-CDs exhibit satisfactory POD-like activity and photothermal conversion capability. A detailed study by spectral analyses demonstrates that the substantial ROS generation is correlated with the advanced structure of Fe-CDs. The in vitro antibacterial experiments suggest that the combination of intrinsic POD-like activity plus local mild heat endows Fe-CDs 99.68% and 99.85% antibacterial ratio against *S. aureus* and *E. coli*, respectively. In addition, the Fe doped and NIR laser irradiation contribute to fibroblast proliferation, neovascularization, and collagen deposition, thus enable the Fe-CDs-mediated healing of bacteria-infected wounds. Almost complete wound healing could be achieved during in vivo therapy. More importantly, Fe-CDs with ultrasmall size showed good biocompatibility without causing substantial inflammatory or pathological damages to normal tissues. Overall, this work would shed light on the future design of carbon dots as the antibiotics-free nanoplatforms for wound disinfection and healing.

Declaration of competing interest

The authors declare that they have no known competing financial interests or personal relationships that could have appeared to influence the work reported in this paper.

CRediT authorship contribution statement

Yunhang Liu: Methodology, Investigation, Visualization, Writing – original draft. **Bolong Xu:** Methodology, Visualization, Data curation. **Mingzhu Lu:** Investigation. **Shanshan Li:** Investigation, Data curation. **Juan Guo:** Investigation. **Fangzhou Chen:** Investigation. **Xiaolu Xiong:** Investigation, Data curation. **Zhe Yin:** Investigation. **Huiyu Liu:** Conceptualization, Project administration, Funding acquisition. **Dongsheng Zhou:** Resources, Supervision, Funding acquisition, Writing – review & editing.

Acknowledgements

This work was supported by the National Natural Science Foundation of China (NO. 21822802, 51772018, and 22061130205); National Key Research and Development Program of China (NO. 2016YFA0201500 and 2018YFC1200100); Fundamental Research Funds for the Central Universities (NO. XK1802-8 and buctrc201915).

Appendix A. Supplementary data

Supplementary data to this article can be found online at https://doi.org/10.1016/j.bioactmat.2021.10.023.

References

[1] Q. Pang, D. Lou, S. Li, G. Wang, B. Qiao, S. Dong, L. Ma, C. Gao, Z. Wu, Smart flexible electronics-integrated wound dressing for real-time monitoring and on-demand treatment of infected wounds, Adv. Sci. 7 (2020) 1902673.

[2] B. Aslam, W. Wang, M.I. Arshad, M. Khurshid, S. Muzammil, M.H. Rasool, M. A. Nisar, R.F. Alvi, M.A. Aslam, M.U. Qamar, M.K.F. Salamat, Z. Baloch, Antibiotic resistance: a rundown of a global crisis, Infect. Drug Resist. 11 (2018) 1645.

[3] L. Gao, J. Zhuang, L. Nie, J. Zhang, Y. Zhang, N. Gu, T. Wang, J. Feng, D. Yang, S. Perrett, X. Yan, Intrinsic peroxidase-like activity of ferromagnetic nanoparticles, Nat. Nanotechnol. 2 (2007) 577–583.

[4] Z. Chen, Z. Wang, J. Ren, X. Qu, Enzyme mimicry for combating bacteria and biofilms, Acc. Chem. Res. 51 (2018) 789–799.

[5] G. Fang, W. Li, X. Shen, J.M. Perez-Aguilar, Y. Chong, X. Gao, Z. Chai, C. Chen, C. Ge, R. Zhou, Differential Pd-nanocrystal facets demonstrate distinct antibacterial activity against Gram-positive and Gram-negative bacteria, Nat. Commun. 9 (2018) 1–9.

[6] J. Xi, G. Wei, L. An, Z. Xu, Z. Xu, L. Fan, L. Gao, Copper/carbon hybrid nanozyme: tuning catalytic activity by the copper state for antibacterial therapy, Nano Lett. 19 (2019) 7645–7654.

[7] L. Gao, Y. Liu, D. Kim, Y. Li, G. Hwang, P.C. Naha, D.P. Cormode, H. Koo, Nanocatalysts promote Streptococcus mutans biofilm matrix degradation and enhance bacterial killing to suppress dental caries in vivo, Biomaterials 101 (2016) 272–284.

[8] F. Cao, L. Zhang, H. Wang, Y. You, Y. Wang, N. Gao, J. Ren, X. Qu, Defect-rich adhesive nanozymes as efficient antibiotics for enhanced bacterial inhibition, Angew. Chem. Int. Ed. 58 (2019) 16236–16242.

[9] H. Sun, N. Gao, K. Dong, J. Ren, X. Qu, Graphene quantum dots-band-aids used for wound disinfection, ACS Nano 8 (2014) 6202–6210.

[10] H. Wang, P. Li, D. Yu, Y. Zhang, Z. Wang, C. Liu, H. Qiu, Z. Liu, J. Ren, X. Qu, Unraveling the enzymatic activity of oxygenated carbon nanotubes and their application in the treatment of bacterial infections, Nano Lett. 18 (2018) 3344–3351.

[11] H. Ding, B. Hu, B. Zhang, H. Zhang, X. Yan, G. Nie, M. Liang, Carbon-based nanozymes for biomedical applications, Nano Res (2020) 1–14.

[12] O. Akhavan, E. Ghaderi, Toxicity of graphene and graphene oxide nanowalls against bacteria, ACS Nano 4 (2010) 5731–5736.

[13] D. Mohanta, S. Patnaik, S. Sood, N. Das, Carbon nanotubes: evaluation of toxicity at biointerfaces, Journal of pharmaceutical analysis 9 (2019) 293–300.

[14] X. Dong, W. Liang, M.J. Meziani, Y.-P. Sun, L. Yang, Carbon dots as potent antimicrobial agents, Theranostics 10 (2020) 671.

[15] M. Liu, H. Zhao, S. Chen, H. Yu, X. Quan, Interface engineering catalytic graphene for smart colorimetric biosensing, ACS Nano 6 (2012) 3142–3151.

[16] J. Zhang, S.-H. Yu, Carbon dots: large-scale synthesis, sensing and bioimaging, Mater. Today 19 (2016) 382–393.

[17] W. Li, Y. Liu, M. Wu, X. Feng, S.A. Redfern, Y. Shang, X. Yong, T. Feng, K. Wu, Z. Liu, Carbon-quantum-dots-loaded ruthenium nanoparticles as an efficient electrocatalyst for hydrogen production in alkaline media, Adv. Mater. 30 (2018) 1800676.

[18] S. Zhuo, Y. Guan, H. Li, J. Fang, P. Zhang, J. Du, C. Zhu, Facile fabrication of fluorescent Fe-doped carbon quantum dots for dopamine sensing and bioimaging application, Analyst 144 (2019) 656–662.

[19] B. Yu, W. Wang, W. Sun, C. Jiang, L. Lu, Defect engineering enables synergistic action of enzyme-mimicking active centers for high-efficiency tumor therapy, J. Am. Chem. Soc. 143 (2021) 8855–8865.

[20] L. Huang, J. Chen, L. Gan, J. Wang, S. Dong, Single-atom nanozymes, Sci. Adv. 5 (2019), eaav5490.

[21] S. Li, L. Shang, B. Xu, S. Wang, K. Gu, Q. Wu, Y. Sun, Q. Zhang, H. Yang, F. Zhang, A nanozyme with photo-enhanced dual enzyme-like activities for deep pancreatic cancer therapy, Angew. Chem. Int. Ed. 58 (2019) 12624–12631.

[22] Y. Cai, J. Fu, Y. Zhou, Y.-C. Chang, Q. Min, J.-J. Zhu, Y. Lin, W. Zhu, Insights on forming N, O-coordinated Cu single-atom catalysts for electrochemical reduction CO 2 to methane, Nat. Commun. 12 (2021) 1–9.

[23] W. Wu, L. Zhan, W. Fan, J. Song, X. Li, Z. Li, R. Wang, J. Zhang, J. Zheng, M. Wu, Cu–N dopants boost electron transfer and photooxidation reactions of carbon dots, Angew. Chem. Int. Ed. 54 (2015) 6540–6544.

[24] D. Zhou, P. Jing, Y. Wang, Y. Zhai, D. Li, Y. Xiong, A.V. Baranov, S. Qu, A. L. Rogach, Carbon dots produced via space-confined vacuum heating: maintaining efficient luminescence in both dispersed and aggregated states, Nanoscale Horiz 4 (2019) 388–395.

[25] Z. Yang, S. Guo, X. Pan, J. Wang, X. Bao, FeN nanoparticles confined in carbon nanotubes for CO hydrogenation, Energy Environ. Sci. 4 (2011) 4500–4503.

[26] B. Geng, D. Yang, D. Pan, L. Wang, F. Zheng, W. Shen, C. Zhang, X. Li, NIR-responsive carbon dots for efficient photothermal cancer therapy at low power densities, Carbon 134 (2018) 153–162.

[27] P. Zimmer, L. Burkhardt, A. Friedrich, J. Steube, A. Neuba, R. Schepper, P. Müller, U. Flörke, M. Huber, S. Lochbrunner, M. Bauer, The connection between NHC ligand count and photophysical properties in Fe (II) photosensitizers: an experimental study, Inorg. Chem. 57 (2018) 360–373.

[28] S. Sun, J. Chen, K. Jiang, Z. Tang, Y. Wang, Z. Li, C. Liu, A. Wu, H. Lin, Ce6-modified carbon dots for multimodal-imaging-guided and single-NIR-laser-triggered photothermal/photodynamic synergistic cancer therapy by reduced irradiation power, ACS Appl. Mater. Interfaces 11 (2019) 5791–5803.

[29] S. Sun, Q. Chen, Z. Tang, C. Liu, Z. Li, A. Wu, H. Lin, Tumor microenvironment stimuli-responsive fluorescence imaging and synergistic cancer therapy by carbon-dot–Cu2+ nanoassemblies, Angew. Chem. Int. Ed. 59 (2020) 21041–21048.

[30] S. Kabir, K. Artyushkova, A. Serov, B. Kiefer, P. Atanassov, Binding energy shifts for nitrogen-containing graphene-based electrocatalysts–experiments and DFT calculations, Surf. Interface Anal. 48 (2016) 293–300.

[31] B.C. Martindale, G.A. Hutton, C.A. Caputo, S. Prantl, R. Godin, J.R. Durrant, E. Reisner, Enhancing light absorption and charge transfer efficiency in carbon dots through graphitization and core nitrogen doping, Angew. Chem. Int. Ed. 56 (2017) 6459–6463.

[32] L. Zhou, P. Fu, Y. Wang, L. Sun, Y. Yuan, Microbe-engaged synthesis of carbon dot-decorated reduced graphene oxide as high-performance oxygen reduction catalysts, J. Mater. Chem. 4 (2016) 7222–7229.

[33] B. Xu, H. Wang, W. Wang, L. Gao, S. Li, X. Pan, H. Wang, H. Yang, X. Meng, Q. Wu, Z. Lirong, S. Chen, X. Shi, K. Fan, X. Yan, H. Liu, A single-atom nanozyme for wound disinfection applications, Angew. Chem. Int. Ed. 58 (2019) 4911–4916.

[34] Y. Yang, X. Wu, L. Ma, C. He, S. Cao, Y. Long, J. Huang, R.D. Rodriguez, C. Cheng, C. Zhao, Bioinspired spiky peroxidase-mimics for localized bacterial capture and synergistic catalytic sterilization, Adv. Mater. 33 (2021) 2005477.

[35] M.S. Kim, J. Lee, H.S. Kim, A. Cho, K.H. Shim, T.N. Le, S.S.A. An, J.W. Han, M. I. Kim, J. Lee, Heme cofactor-resembling Fe–N single site embedded graphene as nanozymes to selectively detect H2O2 with high sensitivity, Adv. Funct. Mater. 30 (2020) 1905410.

[36] C. Wang, H. Wang, B. Xu, H. Liu, Photo-responsive nanozymes: mechanism, activity regulation, and biomedical applications, View 2 (2021) 20200045.

[37] A.E.K. Loo, Y.T. Wong, R. Ho, M. Wasser, T. Du, W.T. Ng, B. Halliwell, Effects of hydrogen peroxide on wound healing in mice in relation to oxidative damage, PLoS One 7 (2012), e49215.

[38] W.C. Hu, M.R. Younis, Y. Zhou, C. Wang, X.H. Xia, In situ fabrication of ultrasmall gold nanoparticles/2D MOFs hybrid as nanozyme for antibacterial therapy, Small 16 (2020) 2000553.

[39] M. Huo, L. Wang, H. Zhang, L. Zhang, Y. Chen, J. Shi, Construction of single-iron-atom nanocatalysts for highly efficient catalytic antibiotics, Small 15 (2019) 1901834.

[40] D. Davies, Understanding biofilm resistance to antibacterial agents, Nat. Rev. Drug Discov. 2 (2003) 114–122.

[41] M. Rodrigues, N. Kosaric, C.A. Bonham, G.C. Gurtner, Wound healing: a cellular perspective, Physiol. Rev. 99 (2019) 665–706.

[42] T.K. Hunt, H. Hopf, Z. Hussain, Physiology of wound healing, Adv. Skin Wound Care 13 (2000) 6.

[43] X. Xu, X. Liu, L. Tan, Z. Cui, X. Yang, S. Zhu, Z. Li, X. Yuan, Y. Zheng, K.W. K. Yeung, Controlled-temperature photothermal and oxidative bacteria killing and acceleration of wound healing by polydopamine-assisted Au-hydroxyapatite nanorods, Acta Biomater. 77 (2018) 352–364.

[44] A. King, S. Balaji, L.D. Le, T.M. Crombleholme, S.G. Keswani, Regenerative wound healing: the role of interleukin-10, Adv. Wound Care 3 (2014) 315–323.

[45] N.T. Le, D.R. Richardson, The role of iron in cell cycle progression and the proliferation of neoplastic cells, Biochim. Biophys. Acta 1603 (2002) 31–46.

[46] P.C. Smith, C. Martínez, J. Martínez, C.A. McCulloch, Role of fibroblast populations in periodontal wound healing and tissue remodeling, Front. Physiol. 10 (2019) 270.

[47] A.A. Khan, P.E. Banwell, M.C. Bakker, P.G. Gillespie, D.A. McGrouther, A. H. Roberts, Topical radiant heating in wound healing: an experimental study in a donor site wound model, Int. Wound J. 1 (2004) 233–240.